Available online at sjuoz.uoz.edu.krd

Science Journal of University of Zakho

Vol. 13, No.3 pp374–387July-September,2025

p-ISSN: 2663-628X
e-ISSN: 2663-6298

THE SYNTHESIS, CHARACTERIZATION, DFT-OPTIMIZATION, BIOLOGICAL ASSAYS, AND HEAVY METAL STUDIES OF A NEW TETRA DENTATE DERIVATIVE LIGAND AND ITS COMPLEXES

Kwestan Namiq Aziz [1, *], and Eman Ibrahim Alsalihi [1]

[1]Department of Chemistry, Faculty of Science and Health, Koya University, Koya, KOY45, Iraq

[*] Corresponding author email: kwestan.200062336248@gmail.com

Received: 11 Apr. 2025 Accepted:18 Jun. 2025 Published:04 Jul. 2025 https://doi.org/10.25271/sjuoz.2025.13.3.1542

ABSTRACT:

A new tetra dentate derivative ligand *[(E)-N-((E)-(2-(((Z)-1-hydroxybutylidene) amino) phenyl) (isopropylimino) methyl) butyrohydrazonic acid*] [N_3O] type has been prepared from the condensation process of equimolar 2-aminobenzohydrazide, isopropyl amine and followed by another addition of butyric acid. Spectroscopic techniques as FT-IR, UV-visible, Mass spectrum, ^{1}H,^{13}C-NMR, T.L.C., Melting point, Conductivity measurements, Magnetic moment, DFT-optimization studies and other methods have been used to characterize the ligand and its new complexes with the general formula $[L(M_2)Cl_3.H_2O]$ (where M= Ni^{II}, Co^{II}, Cu^{II}, Mn^{II}, Cd^{II}, and Zn^{II}). Studying biological activity for the ligand and its complexes against two gram-positive and two gram-negative bacteria. The formed compounds were evaluated for antibacterial activity against two gram-positive and two gram-negative bacteria which are *Staphylococcus aureus*, *Staphylococcus epidermidis*, *Escherichia coli,* and *Pseudomonas aeruginosa.* The developed ligand and its metal complexes performed well versus both kinds of bacteria Scheme 1.

GRAPHICAL ABSTRACT:

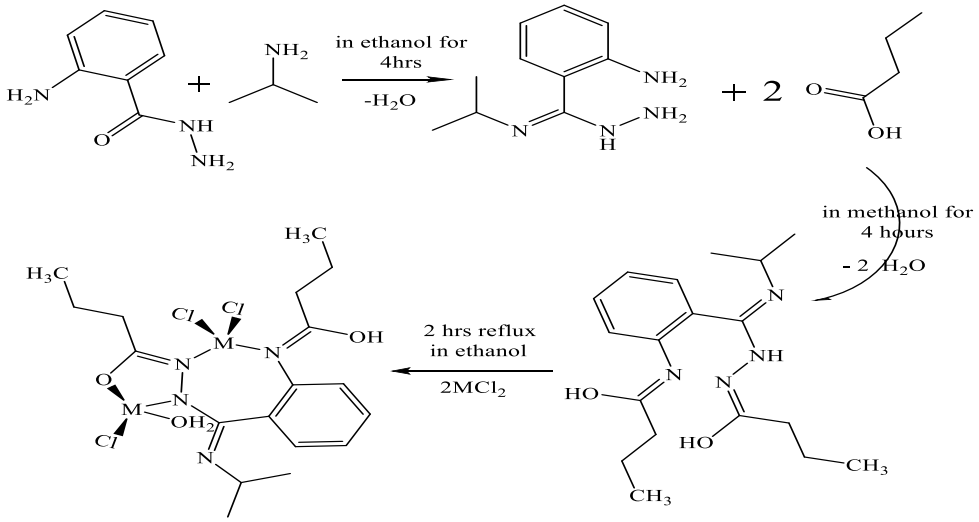

Scheme 1: Graphical Abstract [where M= Ni^{II}, Co^{II}, Cu^{II}, Cd^{II}, Zn^{II}, Mn^{II}]

KEYWORDS: N_3O Ligand, Butyric Acid, Schiff Bases, Wastewater Purification, Antimicrobial Studies, DFT-Optimizatione.

1. INTRODUCTION

A Schiff base is the reaction of condensation between the carbonyl part of an aldehyde or ketone and a primary amine (Abu-Dief & Mohamed, 2015). Imine, anil, and azomethine are various nomenclature for Schiff base, characterized by the $R2C = N -$ functional group (Ghosh, *et al*., 2019). Since Schiff bases have basic properties due to the presence of a n electron pair on the nitrogen atom (Hamad *et al.,* 2024), Coordination chemistry science, analytical chemistry, colors and dyes, the polymer industry, vitamins, and enzymes for model biomolecules are just a few of the various diverse sectors in which they find use. It is commonly recognized that Schiff bases have herbicidal, antifungal medication, and anticancer properties (Nawaz, *et al*., 2020). In addition to their significant roles in

[*] Corresponding author

catalysis and organic synthesis (Abd El-Halim, 2018). Schiff bases can be from to poly dentate ligands that form extremely stable complexes with metals. Hydrazides of carboxylic acids are important chemical molecules that have garnered a lot of interest from scientists. As intermediates in the synthesis of several chemical derivatives, these substances are essential. Hydrazides have the typical chemical formula $RCONHNH_2$, where R stands for an aromatic or aliphatic group that has been substituted or left unsubstituted (Wang, *et al*., 2016). Isopropyl amine is an organic compound that is colourless liquid with an ammonia-like odour, hygroscopic, flammable, miscible with water. Isopropyl amine a basic substance that exhibits the protonation process, acylation, alkylation, and condensing reaction with carbonyls characteristic of other simple alkyl amines, similar to other simple aliphatic amines. Besides being a hair remover, it is also added to petroleum-based materials, used to create insecticides, and regulated in plastics. Isopropyl amine is a building block for the production of many different herbicides and also serves as an intermediate in the organic synthesis of coating materials, dyes, rubber compounds, pharmaceuticals, polymers, textiles, dyes, plastics, insecticides, adhesives, solvents, and other items (Anthony & Kumar, 2015). Butyric acid has the chemical formula $CH_3CH_2CH_2CO_2H$, and it is anaerobic bacteria naturally create butyric acid, a short-chain volatile fatty acid. Butyrate, or butanoates, are butyric acid salts and esters. It is a colourless, oily liquid with an acidic taste and a foul odour, followed by a sweet aftertaste that is comparable to ether. Although the acid is not found in large quantities in nature, its esters are. Butyric acid boils at 164.85°C (Baroi, Gavala, Westermann, & Skiadas, 2017). Butyric acid can be used in various ways such as food, cosmetic, the chemical, and pharmaceutical sectors all make substantial use of butyric acid (Xiao, 2018).

AIM OF THE PROJECT: The aim of this study is to prepare a new tetra dentate ligand and its complexes that form a crystal around metal ions in a tetrahedral geometrical shape (sp^3). And expect that the complexes will find applications in various industries, and medicine.

SYNTHESIS

Experimental - Materials and Methods:

Every chemical used in this project was of the reagent grade and was used exactly as Scharlau,Merck, and Fluka supplied it. The **Infrared (FT-IR)** spectra were done by two universities with two different instruments. The first one in the Koya University genetic center was recorded by using an FT-IR in the frequency of (4000-600 cm^{-1}), other one was at Hawler University, where FT-IR spectra were obtained by using a spectrophotometer range at (4000-400 cm^{-1}) with KBr discs. In the (800–200 nm) region, the Uv-visible was obtained using an Agilent Technologies **UV-visible spectrophotometer**. The ligand field and charge transfer were measured using (1.0 cm) quartz cells, with the ligand and complexes having a concentration of (10^{-3} M) in ethanol. A Bruker BM6 equipment was used to record **magnetic measurements** for complexes at room temperature using Faraday's technique. Using a Buchi **Melting Point** B-540 electrothermal apparatus, it has been measured for all the novel complexes were determined. An AD8000 **conductivity** meter for measuring how well the compounds conduct electricity at (27 °C) a (10^{-3} M) solution of the samples in methanol. The **^{1}H** and **^{13}C NMR** were examined with a Bruker Analytik 300 MHz spectrometer, using tetramethyl silane (TMS) as a reference and deuterated DMSO-d_6 as the solvent. An Agilent 5975C **Mass spectrophotometer** was used to analyse the mass spectrum in DMSO solvent.

Synthesis of Derived Ligand [N3O] Type:

The first step to prepare the $[N_3O]$ derivative ligand starts with 2-aminobenzohydrazide (5.50 g, 36.40 mmol) in (40 ml) of absolute ethanol alcohol, added 5 drops of glacial acetic acid, heated on a hot plate and then mixed with isopropyl amine (2.15 g, 36.31 mmol). After that, the mixture was refluxed and stirred for 4 hours, in 1:1 molar ratio respectively. Evaporated the solution to remove ethanol by oven and left until dried, red crystals have been formed, recrystallized with hot ethanol, (yield 91.2%, 6.31 g), m.p. (118-119°C).

The reaction was followed the second step by the condensation reaction between a (40 ml) methanolic solution of synthesized ligand (5.98 g, 31.10 mmol) and butyric acid (5.49 g, 62.30 mmol) in a 1:2 ratio respectively. Refluxed on a hot plate for 4 hours. Upon evaporating the mother liquor, left until dried and a pale red crystal was obtained. The result of reaction gains (9.30 g) of the derived ligand, (Yield 89.9%), m.p. (81-83°C), the scheme of reaction demonstrates in Scheme 1.

Synthesis of [L(Ni2)Cl3.H2O] Complex:

About (0.60 g, 1.80 mmol) of the new derivative ligand in 20 mL methanol dissolved, and (0.47 g, 3.63 mmol) of $NiCl_2.6H_2O$ salt dissolved in (20 ml) of hot distilled water was added to it, in the ratio of 2:1 metal: ligand respectively. Refluxed for 2 hours to obtain (0.73 g) grey precipitate. (Yield 70.7%), m.p. (288-290 °C).

The remaining complexes have been synthesized similarly as the $[L(Ni_2)Cl_3.H_2O]$ complex, and Table 1 shows the ligand and complexes physical characteristics.

Table 1: Some physical properties of ligand and its complexes

Some physical properties of ligands and its complexes						
No.	Chemical formula	M.wt. (g/mol)	Yield%	M.p.°C	Color	Conductivity
1.	$C_{10}H_{16}N_4$	192.27	91.2	118-119	Brown	-
2.	$C_{18}H_{28}N_4O_2$	332.45	89.8	81-83	Reddish-brown	-
3.	$C_{18}H_{28}Cl_3N_4Ni_2O_3$	572.18	70.7	288-290	Grey	10
4.	$C_{18}H_{28}Cl_3Co_2N_4O_3$	572.66	78.7	>300	Dark-purple	23.3
5.	$C_{18}H_{28}Cl_3Cu_2N_4O_3$	581.89	90.3	>300	Green	17
6.	$C_{18}H_{28}Cl_3Mn_2N_4O_3$	564.67	73.8	264-266	Pale pink	11
7.	$C_{18}H_{28}Cd_2C_{13}N_4O_3$	679.63	86.5	286-288	Pale orange	28
8.	$C_{18}H_{28}Cl_3N_4O_3Zn_2$	585.56	72.3	160-162	Brown	3

CHARACTERIZATION

FT-IR

FT-IR spectrum of the derivative ligand: In the spectrum of isopropyl amine Figure 1-B, two absorption bands at (3350 cm-1) that referred to the stretching vibration of υ(NH2) of the primary amine group (Akkuş Taş, 2024), and in the spectrum of 2-aminobnzohydrazide Figure 1-A displayed strong band at (1680 cm-1) assigned to the stretching vibration of υ(C=O) group (Islam & Mohsin, 2007). The two occurrence peaks were removed from the ligand's spectra. Figure 1-C, and switched with another new peak at (1616 cm-1) belongs to υ(C=N), indicating Schiff base reactions.

From the spectrum of the generated ligand, Figure 1-C, we have been two additional little sharp peaks of (NH_2) amino group at (3441 cm^{-1}), and the butyric acid Figure 1-D displayed a strong band at (1710 cm^{-1}) referred to the stretching vibration of υ(C=O) group, twice again these two peaks has been dispersed in the spectrum of derivative ligand Figure 4-E, and substituted with υ(C=N) stretching at (1653 cm^{-1}) resulting from the Schiff base (Hadi, 2022), interaction for the second time.

FT-IR spectrum of the complexes: In the spectrum of the derivative ligand Figure 2-E, the sharp peak at (1653 cm-1) that assign to the stretching υ(C=N). This band has been migrated to the range's lower frequencies (1637-1523 cm-1) for the NiII, CoII, CuII, MnII, CdII, and ZnII metal ion complexes respectively, Figure 2-F, G, H, I, J, and K in compression with that of the free ligand, resulting from the interaction between the metal and the ligand. Other peaks in the range of (572-510 cm-1) were assigned to stretching υ(M-O). Peaks within the range of (543-415 cm-1) were assigned to stretching υ(M-N). All the peaks have been summarized in Table 2.

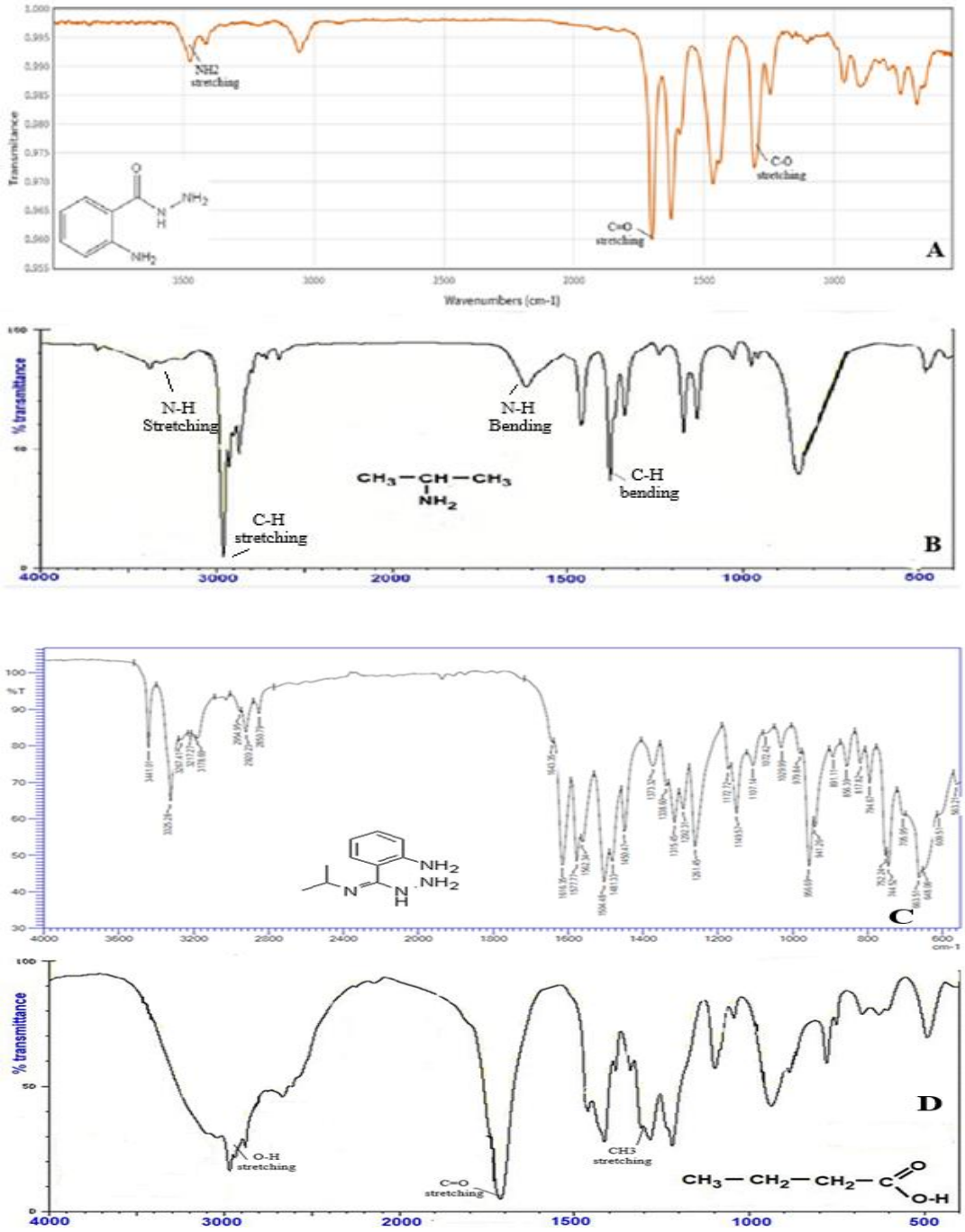

Figure 1: FT-IR spectra of ligand and precursors of it.

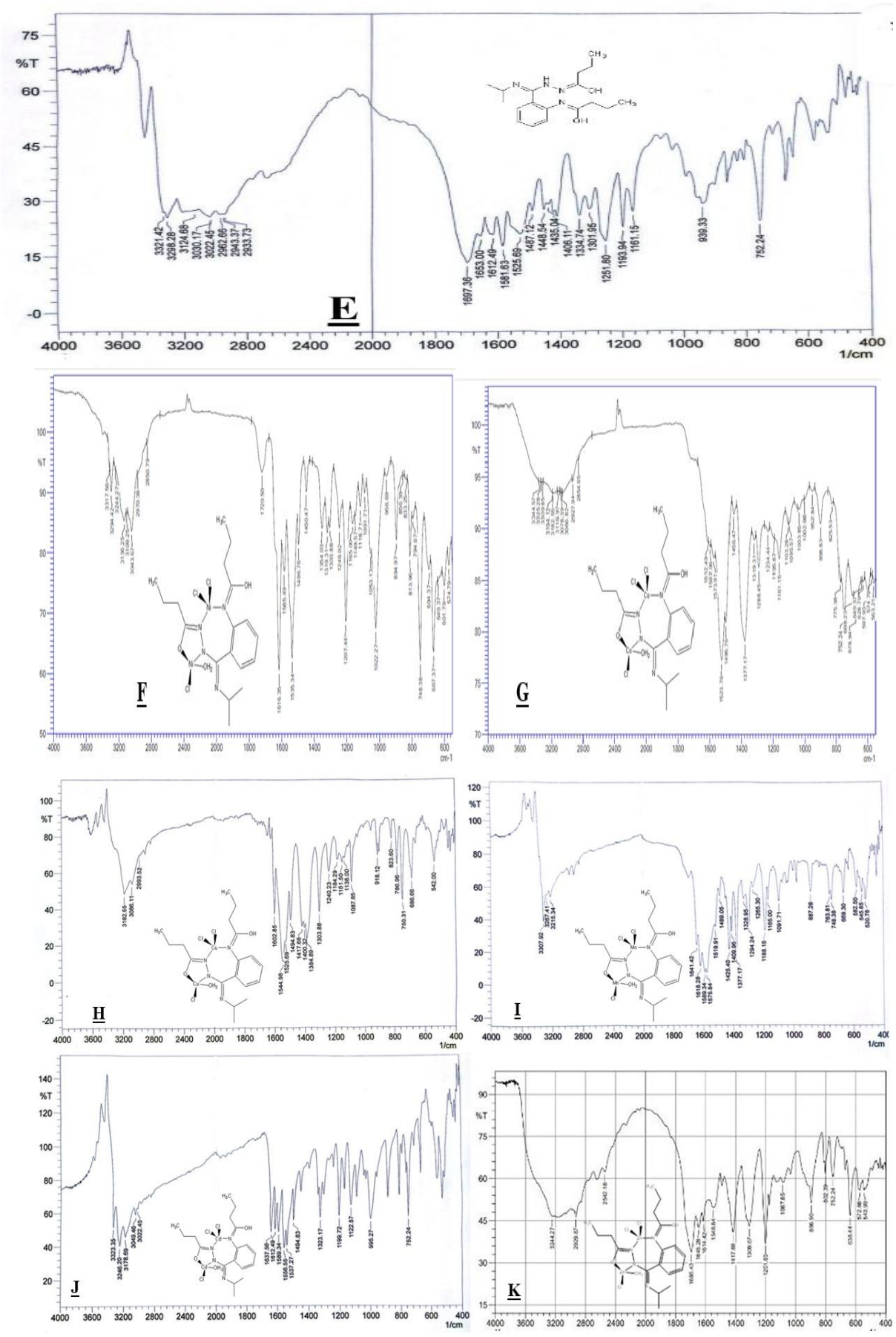

Figure 2: FT-IR spectra derivative ligand and its complex's

Table 2: FT-IR spectral data of the Ligand and its Complex's

Compounds	υ(NH_2)	υ(O-H)	Benzene Ring	υ(C=O)	υ(C=N)	υ(M-O)	υ(M-N)
Isopropyl amine	30800-3100	-	-	-	-	-	-
2-aminobenzohydrazide	3367-3490	-	2870	1680	-	-	-
$C_{10}H_{16}N_4$	3451	-	2777	-	1616	-	-
Butyric acid	-	3300	-	1710	-	-	-
$C_{18}H_{28}N_4O_2$	-	3321	2793	-	1653	-	-
$C_{18}H_{28}Cl_3N_4Ni_2O_3$	-	3317	2850	-	1616	537	418
$C_{18}H_{28}Cl_3Co_2N_4O_3$	-	3344	2927	-	1523	515	416
$C_{18}H_{28}Cl_3Cu_2N_4O_3$	-	3211	2993	-	1602	542	415
$C_{18}H_{28}Cl_3Mn_2N_4O_3$	-	3307	2920	-	1618	520	430
$C_{18}H_{28}Cd_2Cl_3N_4O_3$	-	3246	2799	-	1637	510	425
$C_{18}H_{28}Cl_3N_4O_3Zn_2$	-	3244	2542	-	1614	572	543

UV-Visible Analysis of the Derivative Ligand and its Complexes:

The ligand's spectrum Figure 3-A illustrates a major absorption peak at (241 nm) (41493 cm-1) (∈max=900 molar-1cm-1) assigned to (π→ π*), with a shoulder peak at (342 nm) (29239 cm-1) (∈max=280 molar−1. cm−1) were assigned to (n→ π*) transition.

The same case with the derivative ligand Figure 3-B, that shows a significant absorption peak at (248 nm) (40322 cm^{-1}) (∈max=880 $molar^{-1}cm^{-1}$) assigned to (π→ π*) (Singh, 2021), with a shoulder peak at (345 nm) (28985 cm^{-1}) (∈max=330 $molar^{-1}$. cm^{-1}) were referred to (n→ π*) transition (Kane, *et al.*, 2016).

While the spectrum of the Ni^{II} complex Figure 3-C, includes three peaks at (230 nm) (43478 cm^{-1}) (∈max= 900 $molar^{-1}$. cm^{-1}), (275 nm) (36363 cm^{-1}) (∈max= 380 $molar^{-1}$. cm^{-1}), and (348 nm) (28735 cm^{-1}) (∈max= 150 $molar^{-1}.cm^{-1}$), were tasked with ($\pi \rightarrow \pi^*$), ($n \rightarrow \pi^*$), and charge transfer (*C.T*) transition respectively (Senthilkumar, 2021). Theoretically, three d-d transitions exist $(^3T_1 \rightarrow {}^3T_1(p))$, $(^3T_1 \rightarrow {}^3T_2)$, $(^3T_1 \rightarrow {}^3A_2)$ (Tanabe, 1954), but only peak at (620 nm)(16129 cm^{-1})(∈max=100 $molar^{-1}.cm^{-1}$) represents the high-energy $(^3T_1 \rightarrow {}^3T_1(p))$ band visible region is typically observed due to its intensity and experimental constraints, it is indicating tetrahedral structure around the Ni^{II} metal ion complexes. The lower-energy transitions require specialized techniques for detection. And Co^{+2} complex same as Ni^{+2} have three predicted d-d transitions $(^4A_2 \rightarrow {}^4T_{1(p)})$, $(^4A_2 \rightarrow {}^4T_{2(f)})$, $(^4A_2 \rightarrow {}^4T_{1(f)})$, but only one intense band is observed (Tanabe, 1954). All complexes are shown in Figure 3-D, E, F, G, and H. But only the Zn^{II} and Cd^{II} metal complexes do not included d-d transitions, because the d-orbitals at that case are filled, and there is no possibility for any electronic promotion in d-levels (Reddy, 2007). This peak is related to charge transfer transitions because the metal ion of compounds is a member of the (d10) system (Alsalihi, 2018). Table 3. provides a summary of all peaks.

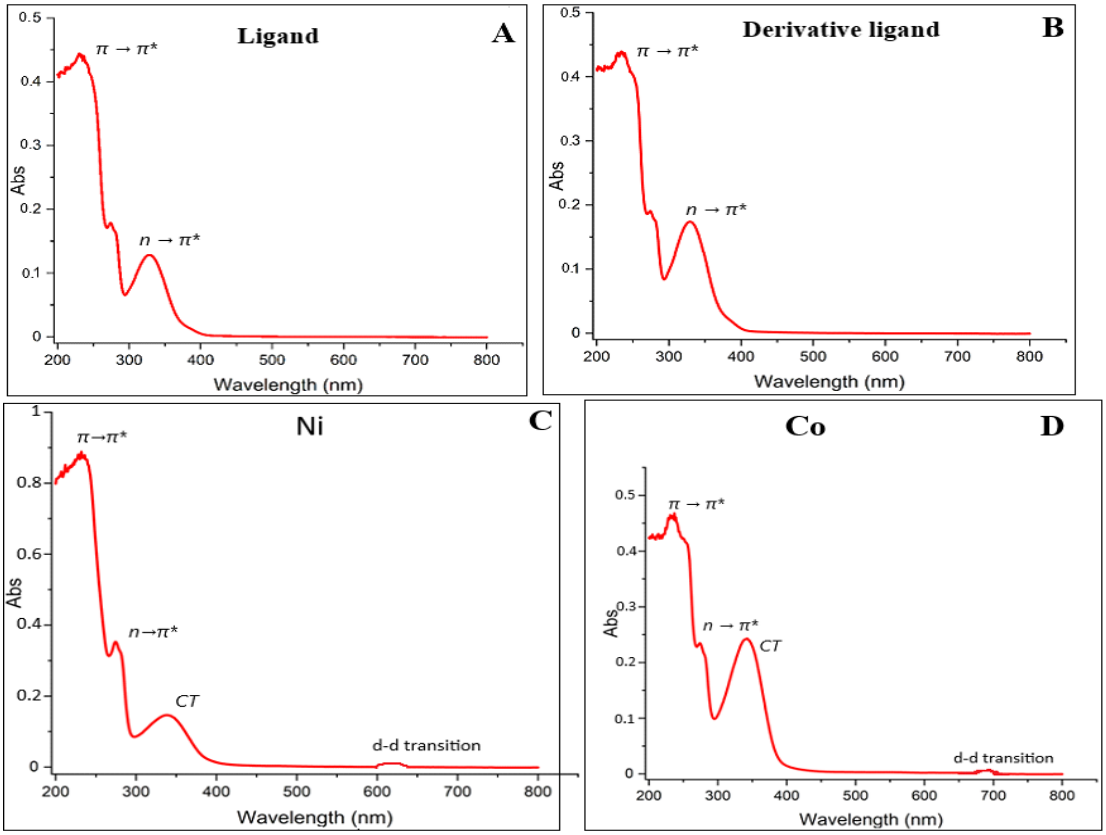

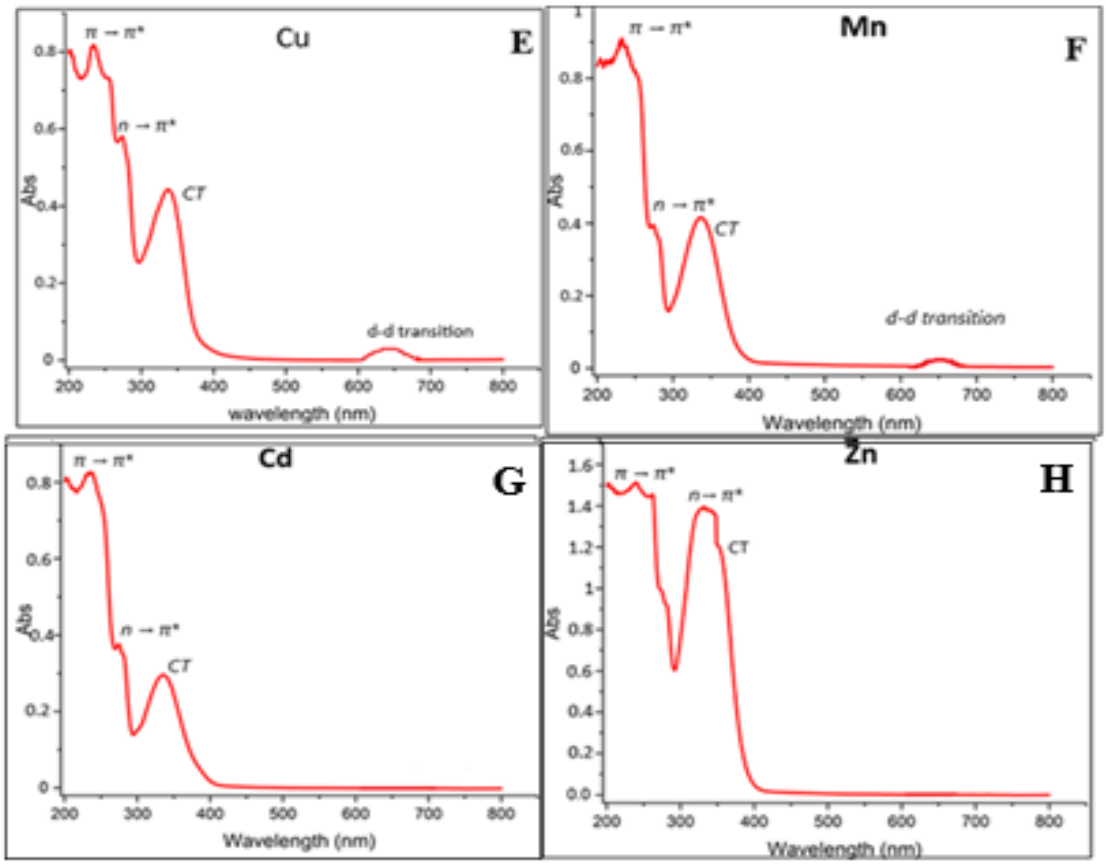

Figure 3: The UV-vis Spectra of the ligand and its complex's

Table 3: The UV-vis spectral data for the ligand and its complexes are explained in.

No.	Compounds	Band Position λ nm	Electronic transition(cm^{-1})	ε max (dm^3. mol^{-1}.cm^{-1})	Assignment	Geometrical shape
1	$C_{10}H_{16}N_4$	241	41493	900	$\pi\rightarrow\pi^*$	-
		342	29239	280	$n\rightarrow\pi^*$	
2	$C_{18}H_{28}N_4O_2$	248	40322	880	$\pi\rightarrow\pi^*$	-
		345	28985	330	$n\rightarrow\pi^*$	
3	$C_{18}H_{28}C_{l3}N_4Ni_2O_3$	230	43478	900	$\pi\rightarrow\pi^*$	Tetrahedral
		275	36363	380	$n\rightarrow\pi^*$	
		348	28735	150	CT	
		620	16129	100	$^3T_1\rightarrow{}^3T_{1(p)}$	
4	$C_{18}H_{28}C_{l3}Co_2N_4O_3$	230	43478	470	$\pi\rightarrow\pi^*$	Tetrahedral
		267	37453	230	$n\rightarrow\pi^*$	
		350	28571	220	CT	
		690	14492	120	$^4A_2\rightarrow{}^4T_{1(p)}$	
5	$C_{18}H_{28}C_{l3}Cu_2N_4O_3$	235	42553	800	$\pi\rightarrow\pi^*$	Tetrahedral
		263	38022	590	$n\rightarrow\pi^*$	
		340	29411	410	CT	
		649	15408	200	$^2E\rightarrow{}^2T_2$	
6	$C_{18}H_{28}C_{l3}Mn_2N_4O_3$	232	43103	910	$\pi\rightarrow\pi^*$	Tetrahedral
		270	37037	400	$n\rightarrow\pi^*$	
		343	29154	390	CT	
		651	15360	110	$^6A_1\rightarrow{}^4T_{1(P)}$	
7	$C_{18}H_{28}Cd_2C_{l3}N_4O_3$	239	41841	820	$\pi\rightarrow\pi^*$	Tetrahedral
		268	37313	370	$n\rightarrow\pi^*$	
		347	28818	300	CT	
8	$C_{18}H_{28}C_{l3}N_4O_3Zn_2$	243	41152	1500	$\pi\rightarrow\pi^*$	Tetrahedral
		350	28571	1330	$n\rightarrow\pi^*$	
		355	28169	1120	CT	

Thin Layer Chromatography:

The T.L.C. measuring technique of the derived ligand and its complexes was done using NiII, CoII, CuII, MnII, CdII, ZnII metal ions in a 10 ml of ethyl acetate and 15 ml of n-hexane mixed solution. The results of the experiment revealed the development of new spots with distinct Rf readings in comparison to the Rf of the derived ligand. Table 4, the spot positions at (5.6 cm), (2.0 cm), (1.1 cm), (5.0 cm), (5.2 cm), and (4.9 cm) of NiII, CoII, CuII, MnII, CdII, ZnII metal ion complexes respectively different from the derived ligand spot position at (7.0 cm) accordingly, which suggests the creation of the complexes and the differences between all of themes indicate it, Figure 4.

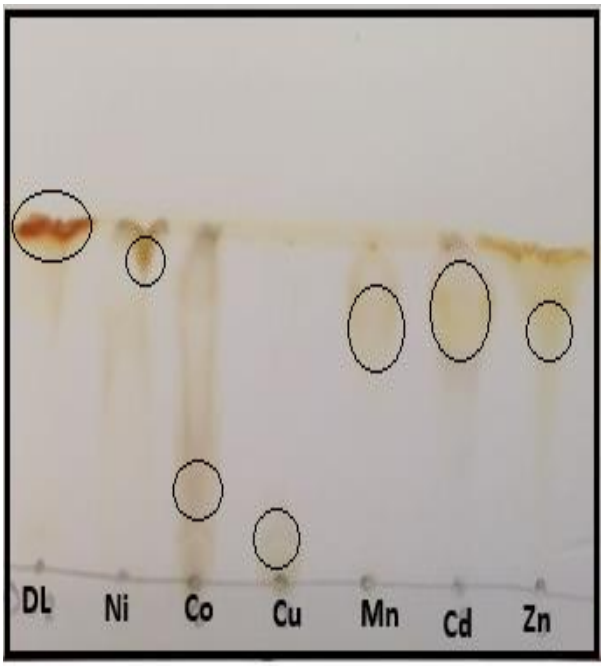

Figure 4: Derivative ligand and its complexes T.L.C. measurement

Table 4: The TLC spot positions for ligand and its metal ion complexes

No.	Compound	Range of R_f
1	$C_{18}H_{28}N_4O_2$	7.0 cm
2	$C_{18}H_{28}Cl_3N_4Ni_2O_3$	5.6 cm
3	$C_{18}H_{28}Cl_3Co_2N_4O_3$	2.0 cm
4	$C_{18}H_{28}Cl_3Cu_2N_4O_3$	1.1 cm
5	$C_{18}H_{28}Cl_3Mn_2N_4O_3$	5.0 cm
6	$C_{18}H_{28}Cd_2Cl_3N_4O_3$	5.2 cm
7	$C_{18}H_{28}Cl_3N_4O_3Zn_2$	4.9 cm

1H-NMR of Derivative Ligand:

Nuclear magnetic resonance spectroscopy was done using DMSO-d6 solvent. Figure 5. Its assignments are detailed in Table 5. and the discussion concerning these assignments is outlined below: The Mass spectrum of [N3O] derivative ligand, exhibited the triplet signal at the range δ (0.9 ppm) corresponding to the (CH3) methyl group proton signal, the doublet signal at the range δ (1.6 ppm) corresponding to the (CH3) methyl group proton signal, the multiplet signal at the range δ (1.44 ppm) due to the (CH2) methylene group, the triplet signal at the range δ (2.11 ppm) due to the (CH2) methylene group, and a singlet signal at δ (2.4 ppm) assigned to (H) proton of DMSO solvent, and a multiplet signal of (CH) at δ (3.3 ppm) of methine group, A singlet signal of (NH) group at δ (5.20 ppm) was caused by the proton of hydrazide. The multiplet signal of the proton of (CH) group ranged between δ (6.50-7.42 ppm) attributed to benzene ring. The broad singlet signal of hydroxyl (OH) group at δ (9.9 ppm) due to alcohol. All the mentioned signals indicate the precise structure of the [N3O] derived ligand (Diab, 2019).

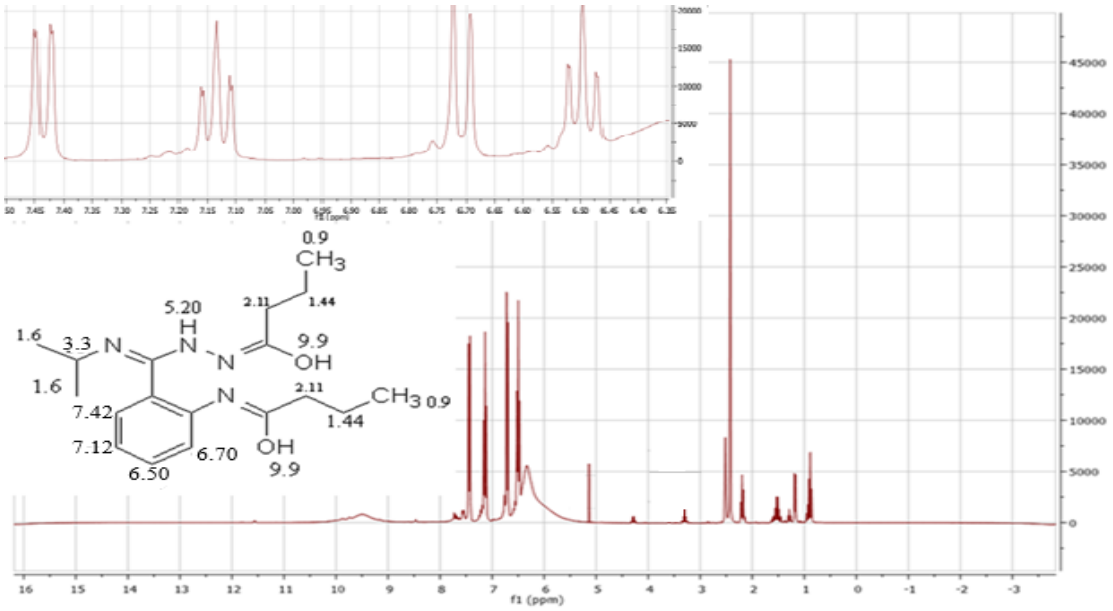

Figure 5: ^{1}H-NMR spectrum of [N_3O] derivative ligand

Table 5: ^{1}H-NMR spectral data for [N_3O] derivative ligand

Proton environment	^{1}H	Splitting	δ (ppm)
Methyl group	2(CH_3)	triplet	0.9
Methyl group	2(CH_3)	doublet	1.6
Methylene group	2(CH_2)	multiplet	1.44
Methylene group	2(CH_2)	triplet	2.11
DMSO solvent	-	-	2.4
methine	1(CH-N)	multiplet	3.3
hydrazide	1(N-H)	singlet	5.20
Benzene ring	1(C-H)	triplet	6.50
Benzene ring	1(C-H)	doublet	6.70
Benzene ring	1(C-H)	triplet	7.12
Benzene ring	1(C-H)	doublet	7.42
Alcohol	2(C-OH)	singlet	9.9

13C HNMR Spectroscopy:

Based on 13C-NMR spectroscopy for [N3O] derivative ligand was done using the DMSO-d6 solvent. The number of signals detected correlates with the existence of magnetically nonequivalent carbon atoms. The signals of (CH3) at range (14.2-21.9 ppm) are attributed to the aliphatic carbon. The signals of the (CH2) group appear at the range (20-37 ppm) due to aliphatic carbon. While the signal of the DMSO solvent appears at (40 ppm). The signal of (C-H) group at (61.8 ppm) were assigned to methine. Six signals at the range δ (113.7-132.6 ppm) corresponding to (C=C) to aromatic carbon of the benzene ring. The bands appear at range between δ (150-175 ppm) is attributed to the azomethine carbon of the (CH=N) group of ligand. These results correspond with those of substances that have been previously distributed, as illustrated in Figure 6. Details of the remaining chemical changes are outlines in Table 6. (Kumagai, 2024).

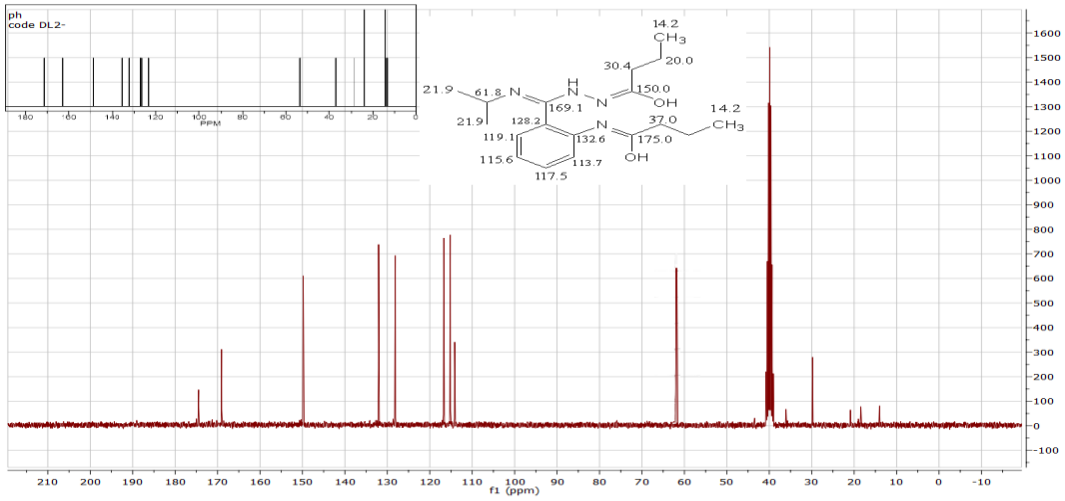

Figure 6: ^{13}C-NMR spectrum of [N_3O] derivative ligand

Table 6: ^{13}C-NMR spectral data for [N_3O] derivative ligand

Group	^{13}C	δ ppm
Aliphatic	4(CH_3)	14.2-21.9
Aliphatic	4(CH_2)	20-37
DMSO solvent	-	40
methine	1(CH-N)	61.8
Benzene ring	4(C-H)	113.7-119.1
Benzene ring	2(C)	128.2-132.6
(CH=N) azomethine	3(C)	150-175

Mass Spectroscopy:

The derivative ligand's mass spectrum Figure 7, illustrates that the parent ion peak corresponds to [M]+ at (m/z=331.2), which aligns closely with the calculated molecular weight of the derivative ligand (332.45 g/mol). This observation further substantiates the superior synthesis and purity of the derivative ligand. All fragment structures are positioned accurately, and the cations and fragments with precise mass are detailed in Table 7 (Lockyer, 2024).

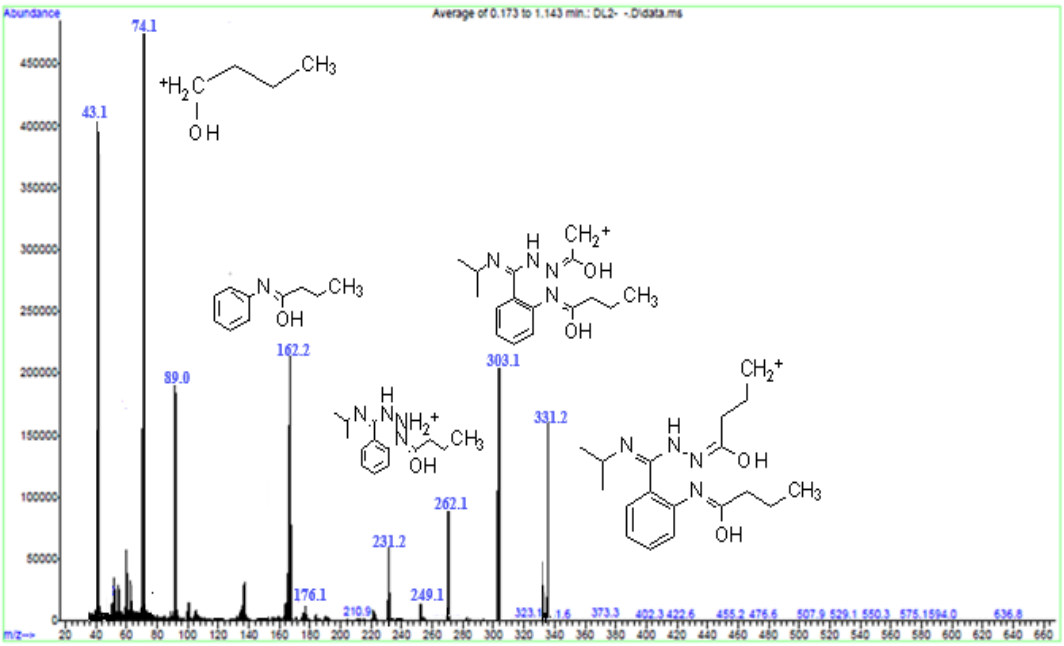

Figure 7: Mass spectrum of the derivative ligand.

Table 7: Mass spectral data of the derivative ligand.

Fragmentations	Exact Mass	Fragmentations (Lost Fragments)
$C_{18}H_{27}N_4O_2^+$	331.21	1H
$C_{16}H_{23}N_4O_2^+$	303.18	CH_2-CH_2
$C_{14}H_{22}N_4O^+$	262.18	CH_2-CH-OH
$C_{14}H_{21}N_3O^+$	247.17	NH_2
$C_{14}H_{19}N_2O^+$	231.15	NH_2
$C_{11}H_{14}NO^+$	176.11	C=N-CH_2-$(CH_2)_2$
$C_{10}H_{12}NO^+$	162.09	CH_2
$C_4H_{10}NO^+$	88.08	C_6H_6
$C_4H_{10}O^+$	74.07	NH_2
$C_3H_7^+$	43.05	CH_2-OH

APPLICATIONS

Conductivity Measurements:

At room temperature, the molar conductance values of complexes were measured in methanol with a 10^{-3} M solution (Aran, 2025). The conductance values were below (50 $Ohm^{-1}.cm^2.mol^{-1}$) of all formed complexes, this indicates that all the complexes are non-electrolytic, Table 8.

Table 8: Molar Conductance data of the complexes

No.	Compounds	Molar conductance (Ohm^{-1} cm^2 mol^{-1})	Behavior
1	$[L(Ni_2)Cl_3.H_2O]$	10	Non-electrolyte
2	[L(Co2)Cl3.H2O]	23.3	Non-electrolyte
3	$[L(Cu_2)Cl_3.H_2O]$	17	Non-electrolyte
4	$[L(Mn_2)Cl_3.H_2O]$	11	Non-electrolyte
5	$[L(Cd_2)Cl_3.H_2O]$	28	Non-electrolyte
6	$[L(Zn_2)Cl_3.H_2O]$	3	Non-electrolyte

Biological activity:

This study is focused on determining inhibitory effect against the development of four different kinds of harmful bacteria of the derivative ligand and its complexes two were gram-positive which are *Staphylococcus aureus* and *Staphylococcus epidermidis*, and the second two were gram-negative which are *Escherichia coli* and *Pseudomonas aeruginosa* (Mukhtar, *et al*., 2021). The biological activity of compounds was studied using the inhibition method (Ali, *et al*., 2022). The derivative ligand and its metal ion complex may serve as bioactive agents for antibacterial action. The disk diffusion technique was employed to perform the experiments. The primary solution was prepared through the mixture of 60 mg of every component in 1 ml of solvent.

N,N-dimethyl sulfoxide (DMSO), and then it was diluted three times in a row. The synthesized ligand exhibited inhibitory activity against Staphylococcus aureus after 24 hours, but not against other types of bacteria, and this inhibitory effect remained consistent after 48 hours. Table 9 illustrates the inhibition diameters of all substances. Moreover, under same experimental conditions with identical types of bacteria, the complexes demonstrated superior efficacy compared to the derivative ligand, as seen in Figure 8.

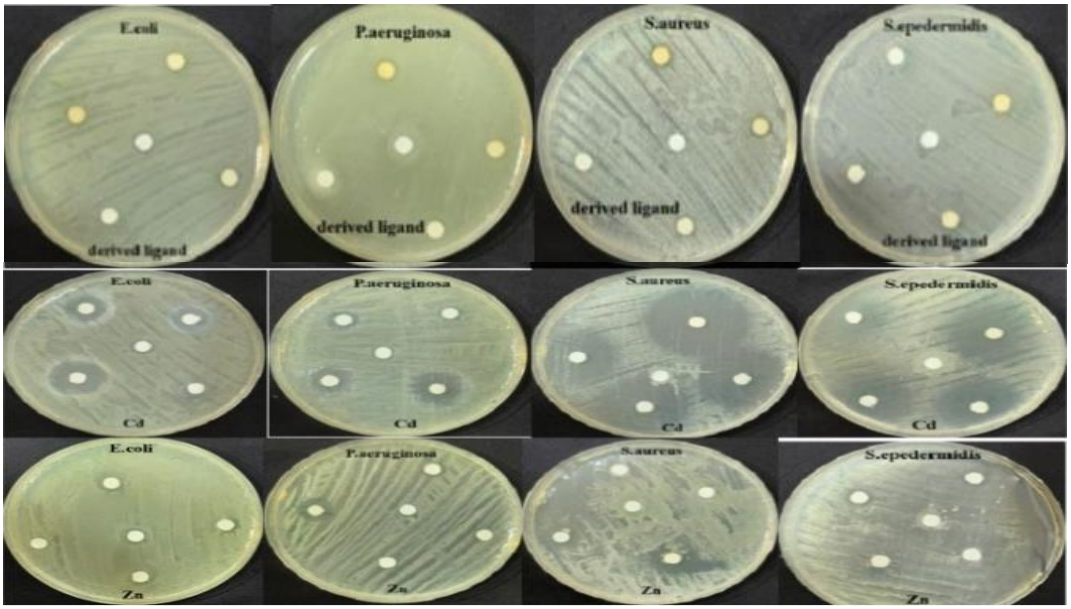

Figure 8: Antibacterial activity of derivative ligand [N_3O] and its complexes

Table 9: Inhibition zone (mm) for antibacterial action

Compounds	Staphylococcus aureus				Staphylococcus epidermidis			
	%100	%50	%25	%12.5	%100	%50	%25	%12.5
$C_{18}H_{28}N_4O_2$	9	8	6	6	-	-	-	-
$C_{18}H_{28}C_{l3}N_4Ni_2O_3$	-	-	-	-	-	-	-	-
$C_{18}H_{28}C_{l3}Co_2N_4O_3$	-	-	-	-	9	6	6	6
$C_{18}H_{28}C_{l3}Cu_2N_4O_3$	-	-	-	-	-	-	-	-
$C_{18}H_{28}C_{l3}Mn_2N_4O_3$	-	-	-	-	-	-	-	-
$C_{18}H_{28}Cd_2C_{l3}N_4O_3$	35	28	26	22	19	15	12	8
$C_{18}H_{28}C_{l3}N_4O_3Zn_2$	16	13	6	6	9	8	7	6
DMSO	-	-	-	-	-	-	-	-
Compounds	Pseudomonas aeruginosa				Escherichia coli			
	%100	%50	%25	%12.5	%100	%50	%25	%12.5
$C_{18}H_{28}N_4O_2$	-	-	-	-	-	-	-	-
$C_{18}H_{28}C_{l3}N_4Ni_2O_3$	7	7	6	6	8	8	7	7
$C_{18}H_{28}C_{l3}Co_2N_4O_3$	-	-	-	-	-	-	-	-
$C_{18}H_{28}C_{l3}Cu_2N_4O_3$	-	-	-	-	-	-	-	-
$C_{18}H_{28}C_{l3}Mn_2N_4O_3$	-	-	-	-	-	-	-	-
$C_{18}H_{28}Cd_2C_{l3}N_4O_3$	17	12	9	7	30	25	22	18
$C_{18}H_{28}C_{l3}N_4O_3Zn_2$	12	9	8	7	13	10	8	6
DMSO	-	-	-	-	-	-	-	-

Magnetic Susceptibility:

The magnetic moment in solid form has been determined by applying Faraday's theory. This allows the number of unpaired electrons to be counted. This should help with the bonding model and electrical structure predictions (Bain, 2008). Table 10. shows the results of measuring the effective magnetic moment (μ_{eff} =*B.M*) after measuring the magnetic susceptibility of a few chosen complexes at room temperature. By Using the formula (μ_{eff} =2.828$\sqrt{XA\,.\,T}$) and according to the calculated μ eff it is demonstrated that some complexes are in a high spin state. The d orbital of Ni^{II} have 2 unpaired electrons and 3 paired electrons, Co^{II} have 3 unpaired electron and 2 paired electrons, Cu^{II} have 1 unpaired electron and 4 paired electrons, Mn^{II} has 5 unpaired electrons, but Cd^{II} and Zn^{II} have not unpaired electrons because they have 10 electrons in d orbital, therefore magnetic moment is equal to zero and doesn't take magnetic susceptibility, Consequently, the hybridization is sp^3, expressing the tetrahedral geometry structure for each complex. The magnetic moment value demonstrates that the complexes are paramagnetic and has high spin except Zinc and Cadmium complexes with low spin and diamagnetic and magnetic moment equal to zero.

$[L(Ni_2)Cl_3{\cdot}H_2O]$ (Ni^{II}, d^8)

Calculated (μ_{eff} = 2.71) is generally slightly lower than the spin-only value (μ_{eff} = 2.83). Tetrahedral Ni^{II} is susceptible to spin-orbit coupling which *reduces* the magnetic moment.

$[L(Co_2)Cl_3{\cdot}H_2O]$ (Co^{II}, d^7)

Calculated (μ_{eff} = 4.09) is generally slightly higher than the spin-only value (μ_{eff}= 3.87). Tetrahedral Co^{II} complexes always exhibit significant orbital angular momentum contribution because the ground state ($^4T_1$) has significant orbital degeneracy. due to orbital contribution in tetrahedral Co^{II} complexes *increase* the magnetic moment well above the spin-only value.

$[L(Cu_2)Cl_3{\cdot}H_2O]$ (Cu^{II}, d^9)

Calculated (μ_{eff} = 1.99) is generally slightly higher than the spin-only value (μ_{eff}= 1.73). This is typical for Cu^{II} complexes and arises from a small orbital angular momentum contribution.

$[L(Mn_2)Cl_3{\cdot}H_2O]$ (Mn^{II}, d^5)

Calculated (μ_{eff} = 5.99) are very close to the spin-only value (μ_{eff}= 5.92). High-spin d^5 (Mn^{II}) ion has spherically symmetric, half-filled shells. This results in negligible orbital angular momentum contribution. Any slight deviation from the spin-only value is usually due to weak spin-orbit coupling effects. The observed values are characteristic of high-spin Mn^{II} in tetrahedral field. The magnetic moments strongly support the suggested tetrahedral geometry for all complexes.

Table 10: Magnetic susceptibility (*B.M*) data of the complexes and suggested structure

Complexes	Xg /10 $^{-6}$ Gram susceptibility	Xm /10^{-3} molar susceptibility	X_A /10^{-3} atom susceptibility	μ_{eff} *B. M* expt.	μ_{eff} *B.M* calc.	Suggested structure
$[L(Ni_2)Cl_3.H_2O]$	5.94	3.40	3.08	2.7-3.2	2.71	Tetrahedral
$[L(Co_2)Cl_3.H_2O]$	12.9	7.37	7.05	3.7-4.3	4.09	Tetrahedral
$[L(Cu_2)Cl_3.H_2O]$	3.42	1.99	1.67	1.7-2.1	1.99	Tetrahedral
$[L(Mn_2)Cl_3.H_2O]$	27.23	15.38	15.05	5.7-6.2	5.99	Tetrahedral

Computational Studies- (DFT-Optimized Geometries)

HOMO-LUMO energies of [N3O] ligand: The LUMO, HOMO, and global properties of the indicated molecule present in Table 11. This data was acquired via the (LanL2DZ) basis set and the DFT/B3LYP theoretical framework. The energy gap denotes the disparity between a molecule's kinetic stability and its chemical reactivity, it including both EHOMO and ELUMO. A molecule possessing A molecule with a substantial HOMO-LUMO gap is considered hard. Less soft, indicating a diminutive size and markedly diminished polarizability. Table 11 shows that this is calculated based on the energy values of the (HOMO) and (LUMO). The negative chemical potentials of -4.7310 and -1.1581, respectively, show that these compounds are stable and do not decompose into their basic components. The HOMO-LUMO energy gap (ΔE = 3.5729 eV) with the LanL2DZ basis set is a crucial parameter that defines the molecule's stability and reactivity, with a larger gap signifying higher stability and lower chemical reactivity (Becke, 1993), The small energy gap with a LanL2DZ basis set indicates that this more flexible basis set can more effectively account for electron correlation, demonstrating significant electronic diffusion from donor to acceptor orbitals . The literature research indicates that systems exhibiting elevated ionization potential and chemical hardness demonstrate reduced reactivity. Soft molecules have greater reactivity than hard molecules owing to their superior electron transfer capacity. The ionization potential (IP = 4.7310 eV) quantifies the energy necessary to extract an electron from the molecule, reflecting its susceptibility to oxidation. Electron affinity (EA = 1.1581 eV) quantifies the energy produced upon the addition of an electron, indicating the molecule's propensity to acquire electrons. The chemical harshness (η = 1.7864eV) indicates the molecule's resistance to alterations in electron density, with elevated values denoting enhanced stability, whereas chemical softness (S = 0.5598 eV^{-1}), its reciprocal, denotes heightened reactivity. A high Electronegativity (χ = 2.9445 eV) for the LanL2DZ basis set indicates a molecule's capacity to attract electrons, hence affecting its interactions with adjacent entities. The electrophilicity index (ω = 2.4267 eV) measures the molecule's propensity for accepting electrons, which is essential for its reactivity (Parr, 1999). The back-donation energy (ΔE = -0.4466 eV) and, the transferred electrons (Δ*N*) exhibit positive values, (ΔN = 3.6224 eV), A positive Δ*N* indicates that the molecules are emitting electrons and signify electron transfer between the ligand and metal center, enhancing complex stability (Akbari, 2024). A high dipole moment the existence of a (LanL2DZ) (6.4156) component in a molecule indicates a significant level of electrical charge polarity (Lundgren, 2016).

Table 11: The quantum chemical parameters for the derivative ligand

Parameters	Values
HOMO (eV)	-4.7310
LUMO (eV)	-1.1581
ΔE (eV)	3.5729
Ionization potential IP"(eV)	4.7310
Electron affinity "EA"(eV)	1.1581
Chemical hardness "η" (eV)	1.7864
Chemical softness "S" (eV−1)	0.5598
Electronegativity "χ" (eV)	2.9445
Chemical potential "μ"(eV)	-2.9445
Electrophilicity "ω" (eV)	2.4267
Nucleophilicity "Nu" (eV-1)	0.4121
ΔE backdonation	-0.4466
Transfer electron fraction ΔN	3.6224
Dipole-moment (Debye)	6.4156

MEP: The Molecular Electrostatic Potential (MEP) map of the ligand explains its charge distribution and potential reactive sites. The MEP was calculated via the (DFT/LanL2DZ) basis set (Chérif, 2024). displaying areas with differing electrical potential. Figure 9 displays a representation of the (MESP) surface, according to Figure 9, The primarily green surface signifies a neutral electrostatic potential, indicating a balanced electron density devoid of notable nucleophilic or electrophilic characteristics.

Small blue portions correspond to electron-deficient areas, potentially serving as electrophilic sites, whereas yellow regions signify electron-rich, nucleophilic sites and red regions indicate high electron density (negative charge concentration). The MEP analysis forecasts ligand-metal interactions and coordination, facilitating comprehension of chemical reactivity and biological activity.

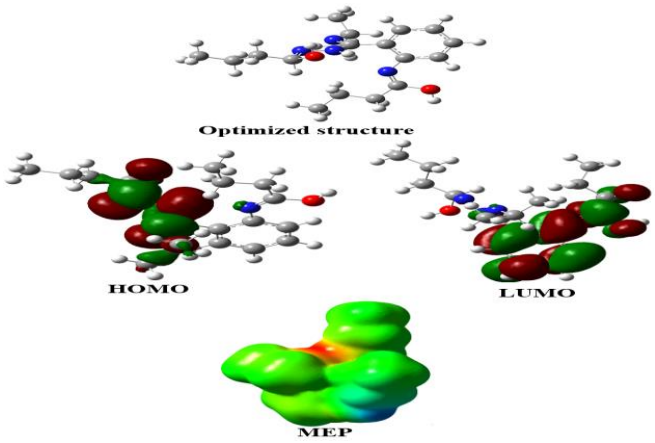

Figure 9: The optimized structure, LUMO, HOMO and MEP for the derivative ligand

Stability Measurement of Derivative Ligand and its Complexes Using UV-Visible Spectroscopy:

The stability of the made derivative ligand and its complexes was checked over time using UV-visible spectroscopy, with the absorbed spectra recorded at different times. The absorbed spectra were recorded at various intervals. The results showed that the UV-visible spectra for the ligand and all the made complexes stayed the same in every test, signifying no notable alteration in the maximum absorption values or variations in peak strength. This consistency indicates that the derivative ligand and its complexes maintain structural integrity and exhibit stability over time under experimental conditions. The lack of spectrum changes indicates the stability of the derivative ligand and its complexes, making it suitable for future applications in coordination chemistry and biological research (Ravichandran, 2014). The stability of the derivative ligand and all six complexes was assessed by measuring absorbance at various time intervals (24 hours, 48 hours, and one, two, and three weeks). No substantial changes in absorbance were observed, affirming its stability. The UV-visible spectra of the derivative ligand and all complexes are shown in Figure 10.

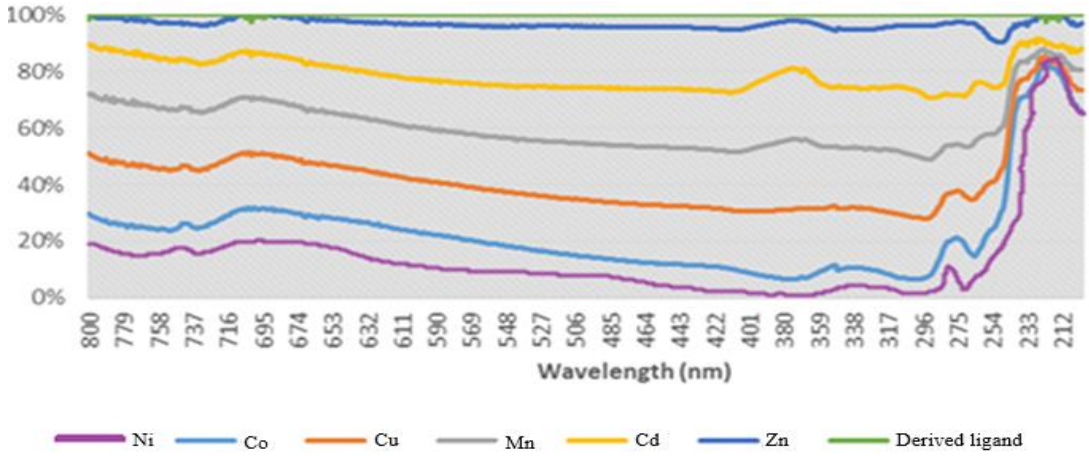

Figure 10: The stability UV-visible spectra of derivative ligand and all complexes.

Wastewater Heavy Metal Removal:

Wastewater contamination is a significant global problem that affects both developed and developing countries. Contaminants in wastewater, such as heavy metals, chemicals, pharmaceuticals, and pathogens, can severely impact the environment, public health, and biodiversity. The removal of lead (Pb) from 0.1 Molar of Pb (CH3COO)2 in 200 ml of D.W and then divided into two containers the first one included just the lead metal ion solution, while the second solution contained the calculated amount from the derivative ligand, forming a brown precipitate by filtration concentration by a specific method in Baghdad University.

[N_3O] type Schiff base derivative ligand is a practical approach for mitigating lead contamination. In this process, the

lead ions in the wastewater, initially at a concentration of 5000 ppm in 100 mL of solution, interact with the derivative ligand to form a complex. After the reaction, the concentration of lead in the solution decreases to 3600 ppm, indicating a reduction of 1400 ppm. This reduction suggests that the derivative ligand has successfully chelated a portion of the lead ions, thus facilitating their removal from the wastewater. The derivative ligand, which typically features nitrogen and oxygen donor atoms, binds to the lead ions, forming a stable complex and reducing the free lead concentration and capturing it in the water by about 26%. This method is a promising strategy for treating contaminated wastewater, highlighting the potential of derivative ligands in environmental cleanup processes (Zaman Brohi, 2020).

CONCLUSION

Spectroscopic analyses confirmed complex formation, with FT-IR spectra showing characteristic shifts indicating derivative ligand coordination. Uv-visible spectra showed distinct peaks in the visible region, confirming d-d transitions and metal ion coordination. Furthermore, the 1H and 13C-NMR analyses corroborated the structure of the derivative ligand. The nature of the fragments in the mass spectrum frequently elucidates the derivative ligand's molecular structure. Measurements of magnetic moments indicate that the geometrical configuration of the complexes is tetrahedral. Conductivity measurements suggest that all complexes are non-electrolytic. Antibacterial studies against two-gram positive bacteria and two-gram negative bacteria revealed enhanced activity of CdII and ZnII complexes over the free derivative ligand. The DFT analysis indicates the HOMO-LUMO and all chemical and physical properties. MEP mapping delineates critical interaction sites for metal coordination and biological function.

Acknowledgement:

I am grateful to Assist. Prof. Dr. Iman Ibrahim, my supervisor, for her support and direction. Many thanks to the head of the chemistry department for their help, and thanks to the assistant of the head of the chemistry department at Koya University.

Ethical Approval:

In this research, we did not address any applications on humans or animals and did not seek support from any institution. Therefor have no moral obligations to others, also, this research is to complete the master's degree in inorganic chemistry. The Ethical Committee of the Koya University, Kurdistan region approved the current research.

Author Contributions:

All authors have reviewed the final version to be published and agreed to be accountable for all aspects of the work. E.I.A., and K.N.A., contributed to the concept and design, acquisition, analysis, or interpretation of data, and drafting of the manuscript.

Funding:
None.

REFERENCES

Abd El-Halim, H. G. (2018). Antimicrobial and anticancer activities of Schiff base ligand and its transition metal mixed ligand complexes with heterocyclic base. Applied Organometallic Chemistry, 32(1), e3899. DOI: https://doi.org/10.1002/aoc.3899

Abu-Dief, A. M., & Mohamed, I. M. (2015). A review on versatile applications of transition metal complexes incorporating Schiff bases. Beni-Suef University *Journal of Basic and Applied Sciences*, 4(2), 119-133. DOI:https://doi.org/10.1016/j.bjbas.2015.05.004

Akbari, Z. C.-D. (2024). Biological evaluation, DFT, MEP, HOMO-LUMO analysis and ensemble docking studies of Zn (II) complexes of bidentate and tetradentate Schiff base ligands as antileukemia agents. *Journal of Molecular Structure*. DOI:https://doi.org/10.1038/s41598-024-54021-z

Akkuş Taş, N. A. (2024). Synthesis, Enzyme Inhibition, and in Silico Studies of Amino Acid Schiff Bases. Iran. J. Chem. Chem. Eng.(IJCCE) Research Article Vol, 43(3). DOI: https://doi.org/10.1117/12.3034192

Ali, A., Pervaiz, M., Saeed, Z., Younas, U., Bashir, R., Ullah, S., . . . Rashid, A. (2022). Synthesis and biological evaluation of 4-dimethylaminobenzaldehyde derivatives of Schiff bases metal complexes: A review. Inorganic Chemistry Communications, 145, 109903. DOI:https://doi.org/10.1016/j.inoche.2022.109903

Alsalihi, E. I.-F. (2018). Synthesis and antibacterial activity of isatin Schiff base derivative with 3-aminoacetophenone and its Ni (II), Co (II) transition metals complexes. ARO-The Scientific *Journal of Koya University*, 6(1), 38-45. DOI:http://dx.doi.org/10.14500/aro.10245

Aran, M. M. (2025). Electrical conductance study of Schiff base in different solvents and temperatures: DFT calculation. Bulletin of the Chemical Society of Ethiopia, 39(1). DOI:10.4314/bcse.v39i1.15

Bain, G. A. (2008). Diamagnetic corrections and Pascal's constants. *Journal of Chemical Education*, 85(4), 532. DOI:https://doi.org/10.1021/ed085p532

Baroi, G. N., Gavala, H. N., Westermann, P., & Skiadas, I. (2017). Fermentative production of butyric acid from wheat straw: Economic evaluation. Industrial Crops and Products, 104, 68-80. DOI:https://doi.org/10.1016/j.indcrop.2017.04.008

Becke, A. D. (1993). Density-functional thermochemistry. III. The role of exact exchange. The *Journal of chemical physics*, 98(7), 5648-5652. DOI:https://doi.org/10.1063/1.464913

Chérif, I. B. (2024). A theoretical and electrochemical impedance spectroscopy study of the adsorption and sensing of selected metal ions by 4-morpholino-7-nitrobenzofuran. Heliyon. DOI:10.1016/j.heliyon.2024.e26709

Diab, M. G. (2019). Sonbati, SM Morgan, S. Abbas, Inner metal complexes of tetradentate Schiff base: Synthesis, characterization, biological activity and molecular docking studies. Applied Organometallic Chemistry, 33(7). DOI:https://doi.org/10.1002/aoc.4945

Ghosh, P., Dey, S. K., Ara, M. H., Karim, K., & Islam, A. (2019). A review on synthesis and versatile applications of some selected Schiff bases with their transition metal complexes. Egyptian *Journal of Chemistry*, 62(Special Issue (Part 2) Innovation in Chemistry), 523-547. DOI: 10.21608/ejchem.2019.13741.1852

Hadi, M. K. (2022). Synthesis, characterization and preliminary antimicrobial evaluation of new schiff bases and aminothiadiazole derivatives of N-substituted phthalimide. Research *Journal of Pharmacy and Technology*, 15(9). DOI:10.52711/0974-360X.2022.00647

Hamad, A. A., Omer, R. A., Kaka, K. N., Abdulkareem, E. I., & Rashid, R. F. (2024). Biological activities of metal complexes with Schiff base. Reviews in Inorganic Chemistry(0). DOI:https://doi.org/10.1515/revic-2024-0075

Islam, M. R., & Mohsin, M. (2007). Synthesis of isatin, 5-chloroisatin and theirΔ-2-1, 3, 4 oxadiazoline derivatives for comparative cytotoxicity study on brine shrimp. ||| Bangladesh *Journal of Pharmacology*, 2(1), 7-12. DOI:https://doi.org/10.3329/bjp.v2i1.494

Kane, C. H., Tinguiano, D., Tamboura, F. B., Thiam, I. E., Barry, A. H., Gaye, M., & Retailleau, P. (2016). Synthesis and

characterization of novel M (II)(M= Mn (II), Ni (II), Cu (II) or Zn (II)) complexes with tridentate N2, O-donor ligand (E)-2-amino-N'-[1-(pyridin-2-yl)-ethylidene] benzohydrazide. Bulletin of the Chemical Society of Ethiopia, 30(1), 101-110. DOI:10.4314/bcse.v30i1.9

Kumagai, S. I. (2024). Solid-state NMR of the retinal protonated Schiff base in microbial rhodopsins. Magnetic Resonance Letters, 4(3). DOI:https://doi.org/10.1016/j.mrl.2024.200132

Kumar, V. V., & Anthony, S. P. (2015). Heavy metal cation and anion sensing studies of N-(2-hydroxybenzyl)-isopropylamine surface functionalized AgNPs. New *Journal of Chemistry*, 39(2), 1308-1314. DOI:DOI https://doi.org/10.1039/C4NJ01740D

Lockyer, N. P.-T. (2024). Secondary ion mass spectrometry. Nature Reviews Methods Primers, 32. DOI:https://doi.org/10.1038/s43586-024-00311-9

Lundgren, R. J. (2016). Key concepts in ligand design: an introduction. Ligand Design in Metal Chemistry: Reactivity and Catalysis, 1-14. DOI:10.1002/9781118839621

Mukhtar, S. S., Hassan, A. S., Morsy, N. M., Hafez, T. S., Hassaneen, H. M., & Saleh, F. M. (2021). Overview on synthesis, reactions, applications, and biological activities of Schiff bases. Egyptian *Journal of Chemistry*, 64(11), 6541-6554. DOI: 10.21608/ejchem.2021.79736.3920

Nawaz, N., Ahmad, I., Darwesh, N. M., Wahab, A., Rahman, S. U., Khan, F. A., . . . Uddin, K. (2020). Synthesis, characterization and antioxidant activity of nickel (II) Schiff base complexes derived from 4-(dimethylamino) benzaldehyde. *Journal of the Chemical Society of Pakistan*, 42(2), 238-242. DOI:https://doi.org/10.1016/j.rechem.2024.101517

Parr, R. G. (1999). Electrophilicity index. *Journal of the American Chemical Society*, 121(9), 1922-1924. DOI:https://doi.org/10.1021/ja983494x

Ravichandran, R. M. (2014). Antioxidant study of quercetin and their metal complex and determination of stability constant by spectrophotometry method. Food chemistry, 472-478. DOI:https://doi.org/10.1016/j.foodchem.2013.09.080

Reddy, K. H. (2007). Bioinorganic chemistry. New Age International. DOI:http://13.232.72.61:8080/jspui/handle/123456789/559

Senthilkumar, S. J. (2021). Synthesis, structure analysis, biological activity and molecular docking studies of some hydrazones derived from 4-aminobenzohydrazide. *Journal of Molecular Structure*, 1226, 129354. DOI:https://doi.org/10.1016/j.molstruc.2020.129354

Singh, G. J. (2021). Synthesis, characterization and UV–visible study of schiff base-acetylene functionalized organosilatrane receptor for the dual detection of Zn2+ and Co2+ ions. Inorganica Chimica Acta, 525. DOI:https://doi.org/10.1016/j.ica.2021.120465

Tanabe, Y. S. (1954). On the absorption spectra of complex ions II. *Journal of the Physical Society of Japan*, 9(5). DOI:https://doi.org/10.1143/JPSJ.9.766

Wang, H.-C., Yan, X.-Q., Yan, T.-L., Li, H.-X., Wang, Z.-C., & Zhu, H.-L. (2016). Design, synthesis and biological evaluation of benzohydrazide derivatives containing dihydropyrazoles as potential EGFR kinase inhibitors. Molecules, 21(8), 1012. DOI:https://doi.org/10.3390/molecules21081012

Xiao, Z. C.-T. (2018). Production of butyric acid from acid hydrolysate of corn husk in fermentation by Clostridium tyrobutyricum: kinetics and process economic analysis. Biotechnology for biofuels, 11. DOI:https://doi.org/10.1186/s13068-018-1165-1

Zaman Brohi, R. O. (2020). Graphene oxide functionalized with a Schiff Base for the removal of Pb (II) ions from contaminated water: experimental and modeling approach. *Journal of Chemical Technology & Biotechnology*, 95(6). DOI:https://doi.org/10.1002/jctb.6362